Structural and magnetic study of zinc-doped magnetite nanoparticles and ferrofluids for hyperthermia applications

P Mendoza Zélis[1], G A Pasquevich[1], S J Stewart[1], M B Fernández van Raap[1], J Aphesteguy[2], I J Bruvera[1], C Laborde[1], B Pianciola[1], S Jacobo[2,3] and F H Sánchez[1,3]

[1]*IFLP-CONICET, CCT-La Plata and Departamento de Física, Facultad de Ciencias Exactas, Universidad Nacional de La Plata, C. C. 67, 1900 La Plata, Argentina*
[2]*INTECIN-CONICET and Departamento de Química, Facultad de Ingeniería, Universidad de Buenos Aires, Av. Paseo Colón 850, C1063ACV Buenos Aires, Argentina*

Abstract

Cubic-like shaped $Zn_xFe_{3-x}O_4$ particles with mean sizes D between 15 and 117 nm were obtained by co-precipitation. Particle size effects and preferential spinel tetrahedral site occupation of Zn^{2+} ions led to noticeable changes of physical properties. $D \geq 30$ nm particles displayed nearly bulk properties, which were dominated by Zn concentration. For $D \leq 30$ nm, dominant magnetic relaxation effects were observed by Mössbauer spectroscopy, being the mean blocking size $D_B \sim 13$ to 15 nm. Saturation magnetization increased with x up to $x \sim 0.1$ - 0.3 due to gradual removal of magnetite neighbouring Fe^{3+} moment cancellation and decreased for larger x due to weakening of superexchange interactions. Power absorbed by water and Chitosan based ferrofluids from a 260 kHz radiofrequency field was measured as a function of x, field amplitude H_0 and ferrofluid concentration. For $H_0 = 41$ kA/m the maximum specific power absorption rate was 367 W/g for $D = 16$ nm and $x = 0.1$. Absorption results could be interpreted within the frame of the linear response theory for $H_0 \leq 41$ kA/m. A departure towards a saturation regime was observed for higher fields. Simulations based on a two levels description of nanoparticle magnetic moment relaxation provided good behavioral agreement with these observations. The frequency factor of the dissipative susceptibility component showed a sharp maximum at $D \sim 16$ nm. This was satisfactorily described by simulations based on moment relaxation processes, which indicated a crossover from Neel to Brown mechanisms at $D \sim 18$ nm. Hints for further improvement of magnetite particles as nanocalefactors for magnetic hyperthermia are discussed.

---

[3] Corresponding authors: sanchez@fisica.unlp.edu.ar, sjacobo@fi.uba.ar

1. Introduction

Magnetic nanoparticles (MNPs) are used in biomedical trials for several diagnosis and therapy applications (Pankhurst et al 2009). Magnetic hyperthermia therapy appears as a promising technique for low invasive treatment of tumors, alone or by improving the efficiency of chemo and radiotherapy. A relatively small increase of temperature of 5 °C – 8 °C produces a large effect on cancer cells viability (Overggard 1989). Magnetic hyperthermia therapy is currently performed in clinical tries by exposing nanoparticles internalized into tumors to a radio frequency (RF) field with amplitude H_0 of the order of $1\ 10^4$ to $2.5\ 10^4$ A/m (Gneveckow et al 2004, Maier-Hauff $et\ al$ 2011). Single domain MNPs absorb power from the field through magnetic relaxation processes and dissipate it into the tumor increasing its temperature, leading to the apoptosis of the tumor cells. The power delivered by MNPs can be varied by changing H_0 and frequency f of the field, but these quantities cannot exceed physiologically imposed limits. It has been reported that parts of the human body with a mean diameter of 0.3 m cannot be exposed without discomfort to RF fields for which the product fH_0 is larger than $5\ 10^8$ A/ms (Brezovich 1987). However, there is a need for new independent determinations of the discomfort factor and also for a general discussion on its definition. In principle it seems reasonable that its value should depend on the particular clinical case as well as on specific treatment variables such as field localization and length of on/off periods. Nevertheless, due to the obvious existence of a discomfort threshold, the enhancement of delivered power relies on the improvement of MNPs performance, which must be achieved bearing in mind that MNPs have to fulfill also biocompatibility and toxicity requirements (Häfeli et al 2007). Ideally the best candidate for effective hyperthermia treatments should be a magnetic material with sufficient biocompatibility, large saturation magnetization, and a Curie temperature (T_C) above, but not too far above, the therapeutic temperature of 42 °C to 45 °C, i.e., able to deliver enough power when temperature T is below the therapeutic one but which switches off when that temperature is reached, therefore avoiding hazardous overheating. Ferrimagnetic iron oxides have the highest saturation magnetization of all known biocompatible materials and have low cost in comparison to other potential choices. Therefore they are the most preferred materials for magnetic hyperthermia, although their ordering temperature is well above the therapeutic one. Magnetite Fe_3O_4 has an ordering temperature of $T_N = 860$ K and a room temperature (RT) saturation magnetization $M_s = 90$ Am^2/kg. It has the cubic inverse spinel structure where two thirds of the ions are Fe^{3+}, half of these occupy A sites (tetrahedral sites) and the other half occupies B sites (octahedral sites). The remaining Fe ions are Fe^{2+} and also occupy B sites.

Doping magnetite with transition metal elements allows the modification of important quantities as saturation magnetization. Here Zn-doped magnetite is prepared and studied as a first

step of a project which foresees further improvement using other soluble additives (Tasaki and Izushi 1977, Behdadfar et al 2012). $Zn_xFe_{3-x}O_4$ ($0 \leq x \leq 0.5$) MNPs and their aqueous based ferrofluid (FF) suspensions have been prepared. A relatively non expensive chemical co-precipitation synthesis route was selected bearing in mind that potential therapeutic applications for the general public demand for low cost materials. Mean MNP sizes and compositions were selected within a wide range of values in order to identify materials parameters intervals in which high specific power absorption rates (SAR) can be obtained (Hergt *et al* 2005). To this end, Zn concentration was varied to search for maximum saturation magnetization M_S. In order to achieve an as complete as possible knowledge of the materials structural, microstructural and magnetic properties, an exhaustive characterization was performed. This kind of system presents effects arising from the variation of size, surface to volume ratio, and Zn concentration which are not easily distinguished from each other, and therefore demands the concurrence of complementary experimental techniques such as TEM, XRD, XAS, Mössbauer effect spectroscopy, and DC magnetometry.

SAR was determined in aqueous FF as a function of Zn content, FF concentration and RF amplitude, and analyzed on the basis of the linear response theory and other models. Its experimental values were correlated with the physical properties of the MNPs.

2. Experimental

2.1 *Sample preparation*

2.1.1 *Series 1 (S1) samples.*

MNPs: Zn-doped magnetite $Zn_xFe_{3-x}O_4$ (x = 0.0, 0.1, 0.2, 0.3, 0.4, 0.5) were obtained following a similar procedure employed in (Vergés *et al* 2008). The $FeSO_4$ precipitation and the subsequent ageing were carried out in a closed system consisting of a three-necked round bottom flasks placed in a water bath with mechanical stirring. The iron (II) solution was introduced at a constant rate under nitrogen flowing. To prepare the undoped magnetite sample nitrogen was bubbled through two solutions independently: (i) 180 ml of distilled water containing NaOH with a final constant concentration of $7.0 \ 10^{-2}$ M and 0.022 M KNO_3; and (ii) 20 ml of $7.4 \ 10^{-1}$ M $FeSO_4.7H_2O$ dissolved in 10^{-2} M H_2SO_4, heated to 70ºC. After 30 minutes, the basic solution was added at a constant rate and under mechanical stirring to the iron (II) sulphate solution. The solution temperature and the nitrogen bubbling rate were kept constant during the synthesis. When the precipitation was completed, nitrogen was allowed to pass for another 5 min. The system was kept at rest inside a water bath at the same temperature for 2 h. At this point, the solution was cooled

down to RT, and the solid was separated by magnetic decantation, washed several times with distilled water and centrifuged. Then, it was dried under vacuum at 40 ℃ for 24 h. For Zn-doped samples $FeSO_4.7H_2O$ was partially replaced by $ZnSO_4.7H_2O$, in a fraction corresponding to the desired composition.

FFs: Washed S1 particles (10 mg) were dispersed in 3.5 ml of a solution containing 2% chitosan and 1% acetic acid, by sonication for 30 min. This FF was purified by centrifugation at 2500 rpm for 10 min and subsequently at 3500 rpm for 15min, at RT.

2.1.2 *Series 2 (S2) samples.*

MNPs: Were prepared with a procedure similar to the followed for S1 samples. The difference lies in step (i) where 180 ml of distilled water were replaced by 100 ml of absolute ethanol and 80 ml of distilled water.

FFs: Washed S2 particles (50mg) were dispersed in 50ml of distilled water by sonication for 12 hs.

2.2 *Sample Characterization*

XRD were performed with a X'Pert diffractometer (Cu$K\alpha$ radiation with λ=1.5406 Å). Data were collected in the 15º ≤ 2θ ≤ 60º range, swept at a rate of 5s per step in 0.02º step scans. Diffractograms were analyzed using MAUD program, which is based on the Rietveld analysis method (Lutterotti 2010).

TEM experiments were carried out using an EM-301 (Philips) microscope, at 100 kV, after a drop of FF was spilled and dried on a carbon-coated copper grid.

Room temperature XANES and EXAFS spectra of the Fe K-edge (7112 eV) and Zn K-edge (9659 eV) were recorded in transmission mode using a Si (111) monochromator at the XAS beamlines of the LNLS (Laboratorio Nacional de Luz Sincrotron) in Campinas, Brazil. The spectra analysis was performed by pre-edge background subtraction followed by a normalization procedure considering the EXAFS region. The fine structure oscillations $\chi(k)$ of each spectrum in the extended region were isolated using the ATHENA program (Ravel and Newville 2005) and Fourier transformed over a specific *k* range.

[57]Fe Mössbauer spectra at 300 K were taken in transmission geometry with a nominal 20 mCi [57]Co source in Rh matrix driven by a triangular velocity wave. Isomer shifts (δ) are referred to metallic α-Fe at RT.

DC Magnetization was recorded vs magnetic field and temperature using vibrating sample magnetometers (maximum applied fields H_{max}= 1190 and 1430 kA/m) and a SQUID (H_{max} = 5570 kA/m) magnetometer.

SAR experiments were conducted in a clear glass Dewar containing 1 ml of FF located at the center of a 5 turns duty coil (25 mm inner diameter). The coil was fed with a 260 kHz ac current. The magnetic field amplitudes H_0 were calculated from the current I through the duty coil. To this end the $H – I$ correlation was determined using a 4 mm diameter thin test coil wound with 20 turns. Field amplitudes of up to 57.7 kA/m were used in order to study SAR dependence on H_0. Temperature was determined with fiber optic sensors in contact with the FF and connected to a calibrated signal conditioner (Neoptix) with an accuracy of $\pm\,0.1$ K. FF temperature was kept below 45 °C in order to minimize FF evaporation and prevent its destabilization. To study SAR dependence on FF concentration, several dilutions up to 1:100 were obtained from samples with typical initial concentrations c of the order of 12 kg (MNP)/m^3 (FF). S1 samples, due to their relatively large MNP mean size, had to be suspended in a Chitosan aqueous solution with viscosity $\eta \sim 6\ 10^{-3}$ Pa s and specific heat $C \sim 4.2\ 10^3$ J/kg K at RT (η and C measured in the present work), in order to ensure FF stability. Instead, S2 samples, having smaller size, could be suspended in water ($\eta \sim 1\ 10^{-3}$ Pa s, $C = 4.18\ 10^3$ J/kg K at RT).

3. Results and Discussion

3.1 XRD and TEM characterization

X-ray diffractograms for S1 and S2 samples are shown in figure 1. They present only Bragg peaks belonging to the cubic spinel structure, indicating that the samples are single phase (JCPDS 19-629).
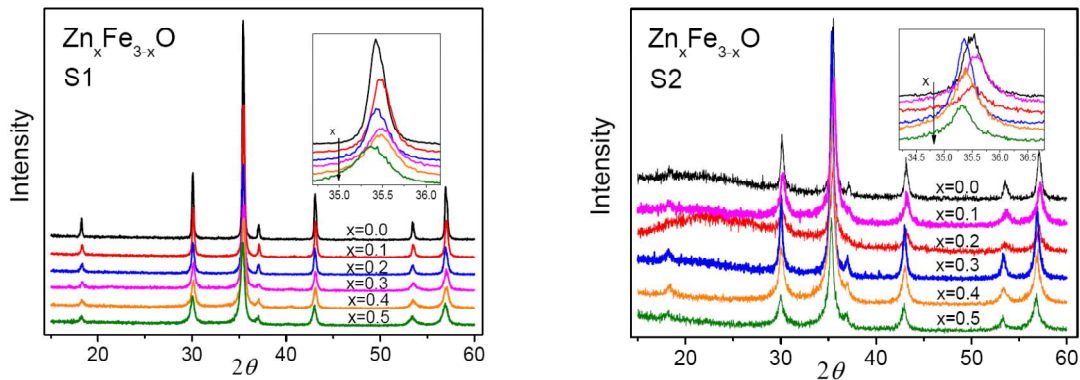

Figure 1. X-ray patterns of Zn-doped magnetite samples S1 and S2. Insets stand for a closer view of the (3 1 1) reflection line.

For each composition the whole spinel pattern (space group *Fd3m*) was refined including peak broadening due to crystallite size and microstrain. For S1 samples, as the zinc concentration *x* increases, the mean crystallite diameter progressively decreases from 117 nm to 26 nm; for S2 samples the *x* decreasing size tendency is not so well defined and mean size ranges between 38 nm for *x* = 0 to 15 nm for *x* = 0.5 (see figure 2). The spinel lattice cell parameter was observed to increase from *x* = 0.0 to *x* = 0.5, in about 0.2 % (0.5 %) for S1 (S2) samples. The shift of (311) reflection line to lower angles due to cell expansion is shown in the inset of figure 1.
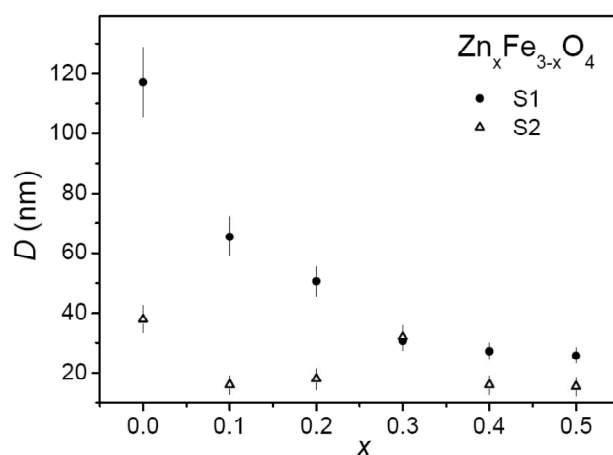

Figure 2. Crystallite size D as a function of Zn concentration for the whole set of samples, obtained after refinement of XRD diffractograms (figure 1) using a Rietveld based code.
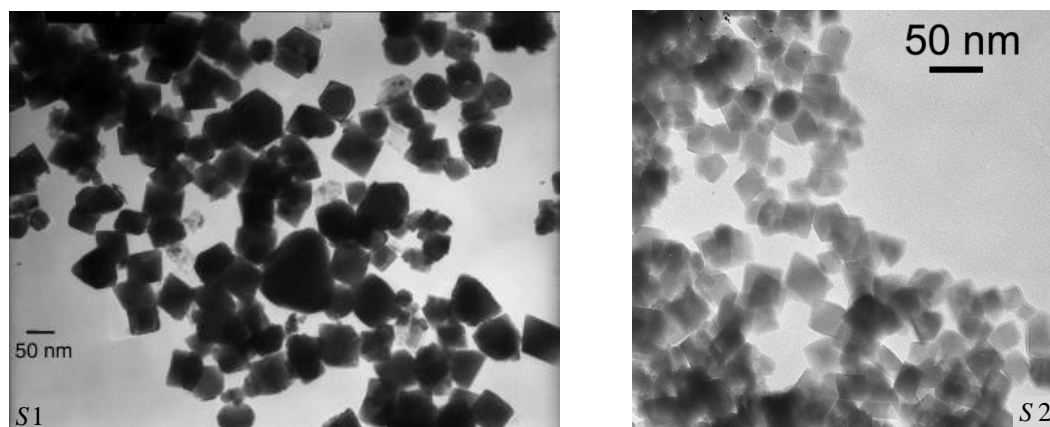

Figure 3. TEM micrographies of samples x = 0.0, D = 117 nm (S1), and x = 0.1, D = 16 nm (S2).

Figure 3 display TEM images of samples *x* = 0.0, *D* = 117 nm (S1) and *x* = 0.1, *D* = 16 nm (S2). The images of all samples showed cubic like nanoparticles and the observed mean sizes were in good agreement with the XRD determinations.

3.2 XAS characterization

The Zn *K*-edge XANES spectrum reflects the electronic $1s{\rightarrow}4p$ transitions of Zn. XANES spectrum of normal $ZnFe_2O_4$ is characterized by peaks at energies (see figure 4) about 9664 (peak A), 9668 (peak B) and 9672 eV (peak C), a shoulder at about 9677 eV (peak D), and an additional contribution at higher energies (peak E) (Nakashima *et al* 2007, Stewart *et al* 2007).
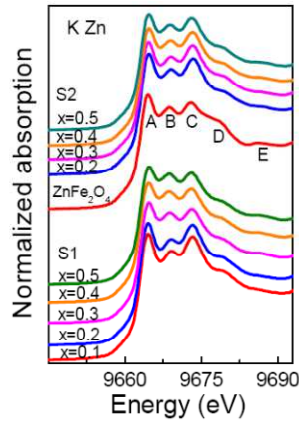

Figure 4. XANES spectra at the Zn K edge of S1 and S2 series, and bulk ZnFe₂O₄.

As depicted in figure 4, all these features are present in the spectra of both series S_1 and S_2. In particular, we do not detect any appreciable increment of the intensity of peak B, which should be noticeable when Zn substitutes Fe at octahedral sites (Nakashima *et al* 2007, Stewart *et al* 2007). We observe that peak B in spectra of S_1 samples $x = 0.1$ and 0.2 is slightly shifted to higher energies. But as the Zn content increases the XANES resembles that of normal $ZnFe_2O_4$. On the contrary, S_2 samples show the same features for all Zn concentrations. Finally, the prominence of peak D in all S_1 and S_2 spectra would indicate that the Zn electronic transitions mainly involve Zn sites with T_d symmetry (Nakashima *et al* 2007).

The Fe K-edge XANES spectra are shown in figure 5 (see also the Supplementary Data, SD). The pre-edge structure arises from electronic $1s{\rightarrow}3d$ quadrupole and $1s{\rightarrow}3d/4p$ dipole transitions. We observe that the pre-edge intensity for series S_1 and S_2 is markedly larger than that observed for normal $ZnFe_2O_4$ but lower than the intensity measured for bulk Fe_3O_4 (figure 5 (c) and (d)). This indicates the presence of Fe atoms occupying both non-centrosymmetric *A* and centrosymmetric *B* sites in Zn-doped magnetite sample (Stewart *et al* 2007). The un-doped samples present the highest peak intensity compatible with a higher *A*-site occupancy of iron ions. For both series, samples $x = 0.2$, 0.3 and 0.4 show similar pre-edge intensities, while the lower pre-edge contribution of $x = 0.5$ would indicate that more Zn ions occupy *A* sites replacing Fe ions. On the other hand, the shift of the edge position to higher energies is more pronounced for $x = 0.3$, 0.4 and 0.5 (S1 series). This is compatible with a tendency towards +3 iron oxidation state as Zn

progressively replaces Fe^{+2} at *A* sites. Features above the edge resemble those of Fe_4O_3 compound (see SD). No other remarkable observations are appreciable that can be correlated with the Zn content, which is expected due to the low Zn:Fe ratio.
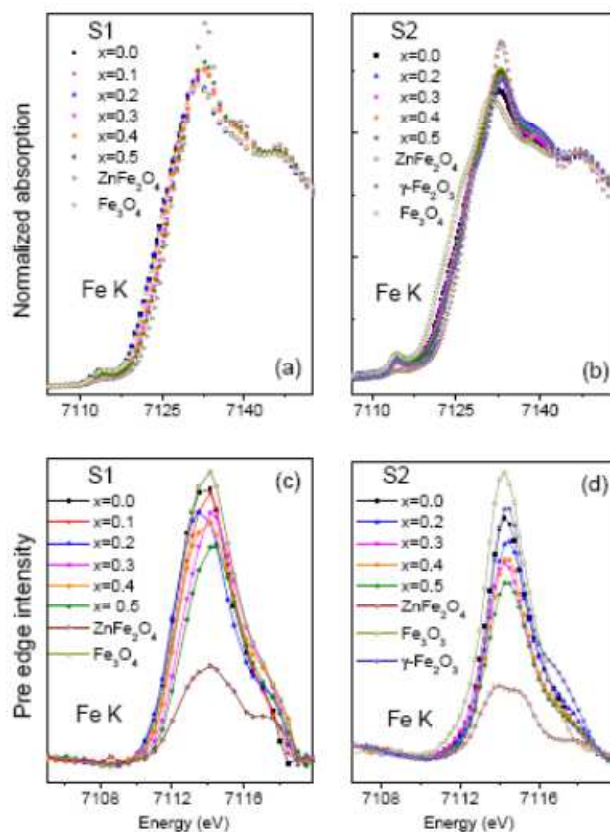

Figure 5. XANES spectra at the Fe K edge of S1 (a), and S2 (b) series. Pre-edge Fe K region after discounting the edge jump contribution of S1 (c) and S2 (d). Spectra of Fe_3O_4, $ZnFe_2O_4$ and γ-Fe_2O_3 bulk compounds are also included for comparison.

The detailed analysis performed on the EXAFS region at Fe and Zn K-edges is included in SD. From these studies we have observed the following: (i) the Fourier transforms (FT) of $\chi(k)$ at Zn K-edge show a reduction of the amplitude of the main peaks when compared to bulk $ZnFe_2O_4$, probably due to the surface disorder, (ii) fitting considering the first coordination shell gave a coordination number *N* near four for Zn central atom (see SD), while *N* of Fe central atom approximates to six when the doping increases; (iii) the typical additional peak that appears in the FT of the Zn K-edge spectrum when Zn occupies *B* sites is absent in all samples.

3.3 Mössbauer effect spectroscopy results

RT Mössbauer spectra are shown in figure 6. In both series a gradual change from bulk-like to magnetically relaxed and/or compositionally disordered states is observed as a function of *x*. Absorption lines broaden while the spectral central contribution grows as Zn content increases. The
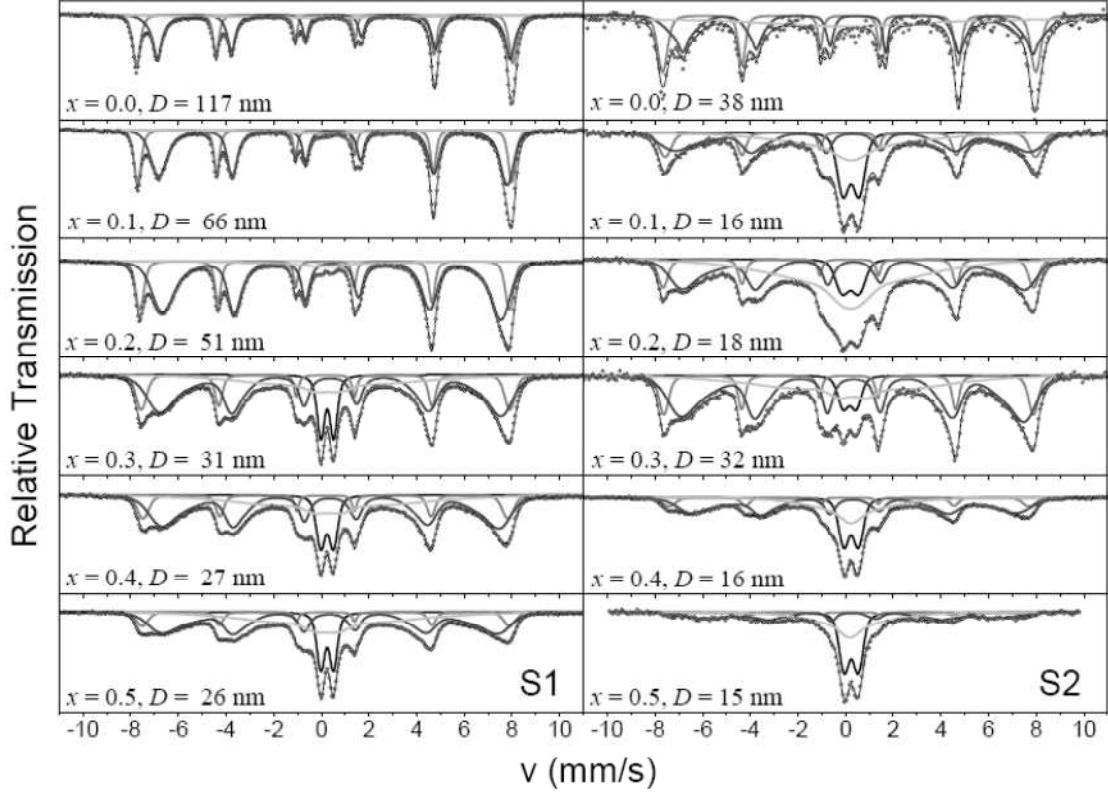

Figure 6: RT Mössbauer spectra and fitted curves for S1 and S2 Zn-doped magnetite MNP. Circles: experimental data. Lines: thin black (fit), dark gray (site B), medium grey (site A), light grey (relaxing), thick black (fast relaxing). For each case Zn content x and mean MNP size is indicated.

$x = 0.0$ spectra display two well resolved magnetic subspectra, especially for the $D = 117$ nm sample (S1), with magnetic hyperfine fields B_{hf} of 49.0 ± 0.1 and 46.0 ± 0.1 Tesla, isomer shifts δ of 0.26 ± 0.01 and 0.63 ± 0.01 mm/s, and nearly null quadruple shift ε, in good agreement with bulk magnetite parameters (Vandenberghe *et al* 2000). The narrower sextet with the larger B_{hf} and the smaller δ is associated with high spin Fe^{3+} ions occupying the *A* sites of the spinel structure, while the other one is assigned to Fe^{3+}/Fe^{2+} ions occupying the *B* sites. The *B* site Fe ions signal broadens as *x* increases, i.e. the B_{hf} distribution at *B* sites broadens as a consequence of the gradual incorporation of Zn^{2+} at *A* sites and the development of different metal ions configurations around *B* sites.

For the theoretical Mössbauer spectra, Voigtian line shapes (Lorentizian lines of constant width Γ = 0.21 mm/s and Gaussian distributions of variable dispersion σ) were assumed. A consistent fit of the whole set of spectra was achieved using a model consisting of one magnetic interaction associated to *A*-site, two magnetic interactions associated to *B*-site with different distribution widths but restricted to have equal hyperfine parameters correlations, a partially resolved sextet associated to Fe probes experiencing relaxation times $\tau \sim 1/f_L$ (slow relaxing component), and a doublet related to probes with $\tau < 1/f_L$ (fast relaxing component), where f_L is the Larmor frequency.

The comparison of the two series spectra allows us to distinguish between the influences of particle size and Zn concentration, bearing in mind the following arguments: (i) particle size diminution leads to increasing relaxation effects due to the reduction of anisotropy energy barriers between MNPs magnetic moment opposite direction states; (ii) Zn addition increases relaxation effects via *A-B* exchange coupling weakening but also induces line broadening due to the increase of chemical disorder, especially around Fe ions at *B* sites. It can be observed that S1 spectra are better resolved than S2 ones for any composition, due to the particle size effect. In S2 results, can be observed that relaxation effects are larger for x = 0.2 than for x = 0.3, indicating that for this particular case the particle size variation (from 18 nm to 32 nm) effect is more important than the Zn concentration increment *(Δx = 0.1)* effect in which concerns to MNP magnetic moment relaxation. A common feature emerging from both series is that relaxation effects involve an important fraction of probes for mean particle sizes of the order of 32 nm or smaller, while for larger mean sizes these effects are minor. From the behaviour of the fast relaxing component relative area (figure 6, doublet subspectrum) it can be estimated that the mean MNP blocking size D_B should be of the order 13 - 15 nm at RT, i.e. the size at which the well resolved and the fast relaxing components contribute with similar areas (see figure 7). For this estimation it has been taken into account that the slow relaxing component corresponds to particles whose sizes are of the order of the blocking size D_B. The Mössbauer effect time window is given by the inverse of the Larmor frequency $f_L \sim 0.3\ 10^8\ \mathrm{s}^{-1}$ of the ^{57}Fe nuclear spin in magnetite. Assuming a Néel relaxation mechanism with a time of attempts $\tau_0 \sim 10^{-9}$ s (Fortin *et al* 2008, Hergt *et al* 2006) and an effective anisotropy energy density K = 1.89 10^4 J/m^3 (Fiorani *et al* 2002), the magnetic core mean blocking size of our magnetite MNP can be estimated as $D_C = \left[(kT/K)\ln\left(1/f_L\tau\right)\right]^{1/3} \approx 9.5\,\mathrm{nm}$. By considering the existence of a surface "dead layer" of thickness $t \sim 2.0 - 2.5$ nm (Kaiser and Miskolczy 1970, Kim *et al* 2001, Knobel *et al* 2008), a MNP total size $D \approx D_C + t \approx 13.5 - 14.5\,\mathrm{nm}$ is obtained, in good agreement with our previous estimation.

When x increases and/or D decreases it is observed that: (i) The relative area of the well
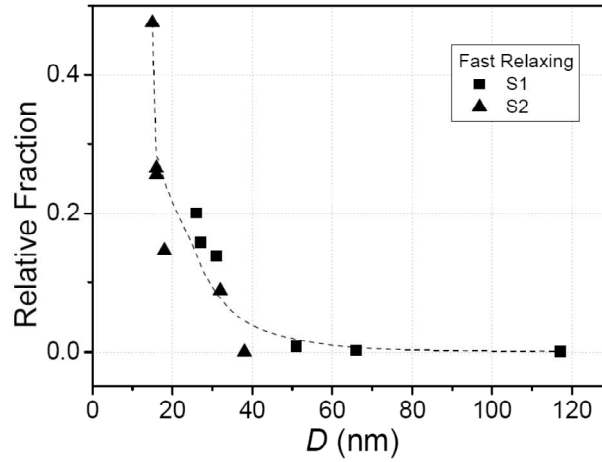

Figure 7. Normalized Mössbauer relative area fractions of the contributions coming from fast relaxing sites as a function of crystallite size for S1 and S2 samples. Normalization is done with respect to the sum of fast relaxing and non relaxing components areas. The dashed line is a guide to the eye.
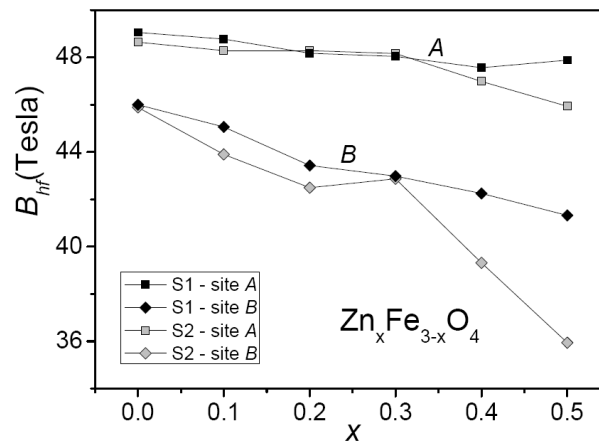

Figure 8. Mean B_{hf} values of the A and B sites contributions as a function of x for S1 and S2 samples.

resolved component originated in A-site Fe probes decreases rapidly while its corresponding B_{hf} reduces at a much slower rate (see figure 8). (ii) As D decreases from 38 nm downward the fast relaxing component spectral area increases steadily (see figure 7). For $D \geq 38$ nm the relative value of the two relaxing components area amounts to a total of only 10 % – 15 % and corresponds almost exclusively to the slow relaxing contribution. (iii) Hyperfine parameters associated to B sites are strongly affected by Zn addition and their absorption lines broaden considerably with x (see figure 6).

For samples with $x \geq 0.3$ or $D \leq 32$ nm the relaxation effects become dominant: the area of the slow relaxing component increases dramatically, as well as that of the fast relaxing one (figure 7) which develops into a central doublet (figure 6). This last interaction is characterized by mean

values of quadrupole splitting $\Delta = 0.535$ mm/s, $\delta = 0.35$ mm/s, and $\sigma = 0.24$ mm/s. Though mean B_{hf} corresponding to both A and B sites decrease with zinc content, the reduction is much more pronounced for site B (figure 8). The coexistence of the magnetically split contributions along with the doublet indicates the simultaneous presence of blocked and unblocked MNP moments. This analysis in terms of blocked and unblocked MNP moments is consistent with the theoretical estimation of the maximum linear dimensions of single-domain magnetite particles, which is of the order of 130 nm (Sorensen 2001), i.e., beyond the crystallite size range of our samples.

The iron ions distribution amongst interstitial A and B sites in the magnetite spinel structure can be depicted as $\left(Fe^{3+}\right)_A\left[Fe^{2+}Fe^{3+}\right]_B O_4^{-2}$. When doping with zinc at the A site the spinel structure $\left(Zn_x^{2+}Fe_{1-x}^{3+}\right)_A\left[Fe_{1-x}^{2+}Fe_{1+x}^{3+}\right]_B O_4^{-2}$ is formed. The Zn^{2+} coordination is characteristic of covalent structures with sp^3 hybridized orbitals. As each Fe^{3+} or Fe^{2+} at B-sites has six nearest-neighbour metal ions at A sites, the B-site Mössbauer lineshape can be considered as a superposition of components arising from different nearest neighbour A-site configurations (Vandenberghe and de Grave 1989). The addition of each Zn^{2+} ion at an A site breaks four Fe(A)-O-Fe[B] superexchange paths. For each broken A-B path B_{hf}^B should decrease resulting in a broadening of the B sites spectral contribution. On the contrary, the effect of broken paths on B_{hf}^A is expected to be much smaller due to the lower contribution from supertransferred B_{hf} (Vandenberghe and de Grave 1989). Therefore, the reduction of B_{hf}^B mean value, the broadening of its distribution, and the decrease of the relative area of the A-site signal with doping, all features observed in our spectra, can be related to the inclusion of Zn^{2+} at A sites replacing Fe^{3+} ions. In order to maintain charge neutrality some oxygen vacancies must be generated or a fraction of Fe^{2+} must be transformed into Fe^{3+}, as proposed by Wen et al. (Wen *et al* 2006) to occur in their $Zn_xFe_{3-x}O_4$ samples prepared by chemical coprecipitation. In figure 9 we observe that while δ_A remains almost unaltered when doping with zinc, the average δ_B decreases monotonically from 0.52 to 0.35 mm/s, indicating that an increasing fraction of iron ions at B-sites change its valence from 2+ to 3+. δ values corresponding to the slow relaxing contribution are similar to those of iron at B sites for the whole concentration range, whereas the fast relaxing component presents δ values intermediate between δ_A and δ_B ones. Assuming that the slow and fast relaxing components correspond to iron at B, and at both A and B – sites, respectively, which is an assumption based on the δ behaviour displayed in figure 9 for S1 samples, we have estimated the relative fraction of total Fe in B and A sites. The results are shown in figure 10,
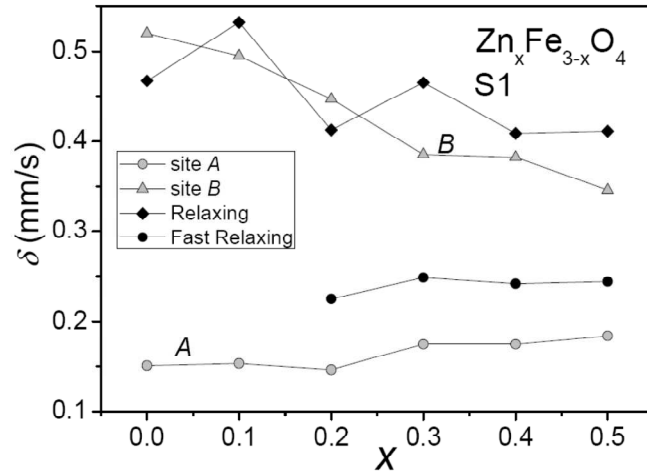
Figure 9. δ values of the contributions coming from different sites as a function of x for S1 samples.

where it can be noted that for $x = 0.0$ the areas ratio B/A are the closest to the value of 2 ideally expected for Fe_3O_4 structure. The relative fractions of Fe ions at A and B sites calculated by assuming that Zn enters exclusively the A site are represented by the dashed lines which follow closely the experimental data. The relaxing contributions are originated in the superparamagnetic behaviour of the smallest particles whose fraction presents an overall growing trend with decreasing x. As stated before, it cannot be completely ruled out that relaxation may also originate from A-B super exchange path interruptions due to the presence of non-magnetic Zn^{2+} ions at A sites, which along with an statistical distribution of Zn^{2+}, would bring about magnetic clusters which undergo also spin relaxation and superparamagnetism.
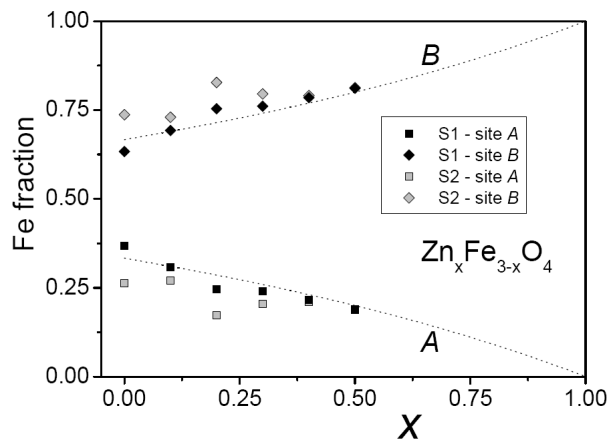

Figure 10. Total Fe fractions in A and B spinel sites as a function of x retrieved from spectra analysis for sets S1 and S2. The dashed lines are the fractions calculated assuming that Zn enters exclusively at the spinel site A.

3.4 DC magnetic studies

The field dependence of the magnetization recorded at 300 K is shown in figure 11. We observe that adding Zn^{2+} ions modifies the MNP ferrimagnetic response producing maximum saturation values of $Ms^{(4)}$ at $x = 0.1$ for S1 ($Ms(0.1)/Ms(0.0) \sim 1.11$) and at $x = 0.3$ for S2 ($Ms(0.3)/Ms(0.0) \sim 1.49$). Saturation magnetization increase was interpreted in terms of elimination
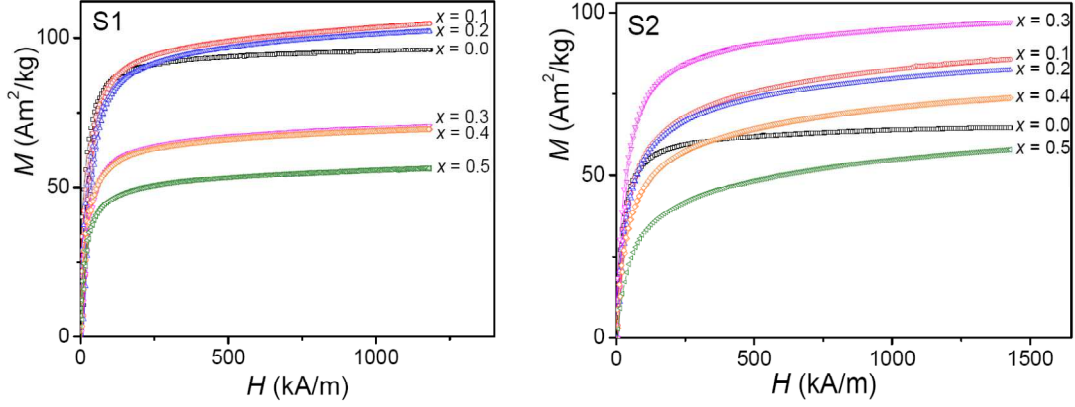

Figure 11. M-H loops taken at 300 K for sets S1 and S2.Only the first quadrant is shown for the sake of clarity.

of Fe^{3+} moment cancellation at neighbouring *A* and *B* sites, since Zn^{2+} incorporation at *A* sites locally switches off *A-B* superexchange. Therefore a net moment of 10 Bohr magnetons (μ_B) appears at the unit formula where Zn^{2+} has been incorporated, instead of the 4 μ_B of pure magnetite.

$Ms(x)$ drops fast for higher *x* and has its minimum at $x = 0.5$ for both series of samples ($Ms(0.5)/Ms(0.1) \sim 0.54$ for S1 an $Ms(0.5)/Ms(0.3) \sim 0.63$ for S2). A similar behaviour is found for the dependence of the coercive field H_C on *x* (figure 12b). The reduction of $Ms(x)$ for $x \geq 0.3$ is mostly
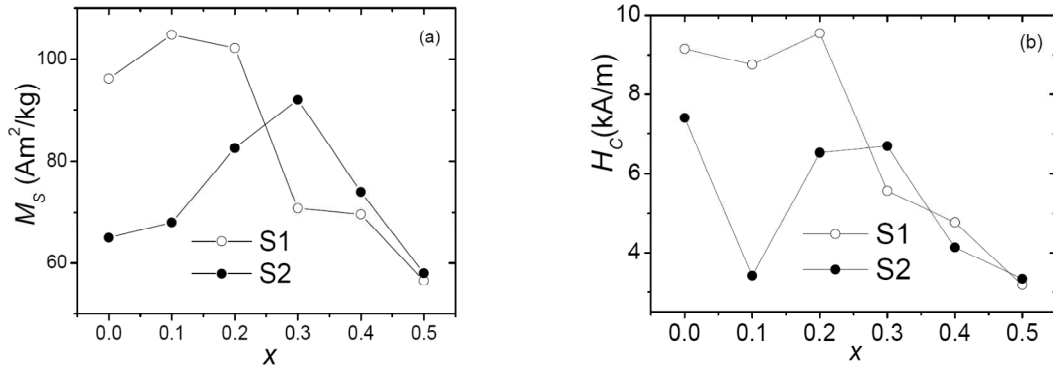

Figure 12.(a) Room temperature magnetization M_s at 1200 kA/m for sets S1 and S2, as a function of x.(b) Coercive field H_c for sets S1 and S2, as a function of x.

---

[4] For simplicity we refer as *Ms* to the value of *M* obtained for the maximum applied fields during the *M* vs *H* experiments, although saturation has not been fully achieved at those fields.

a compositional effect, related to changes in A and B sites Fe population which may modify the resulting average moment. It follows from further weakening of the $A - B$ superexchange interaction and the consequent takeover of the $B - B$ one when Zn^{2+} A site occupation is sufficiently high, thus leading to null atomic moment at the unit formula where Zn^{2+} is located. Size variations have a secondary effect on the observed M_S change, particularly on M_S drop occurring for $x \geq 0.3$, since, as shown in figure 2, crystallite size changes of are less pronounced within this composition range.

3.5 SAR and related studies

Magnetic hyperthermia relies on the ability of MNPs to absorb power from a RF field. This property is expressed by the magnitude defined as SAR which is the power absorbed per unit mass of MNPs[5]. SAR depends on RF field quantities, namely amplitude and frequency. It is also a function of MNP variables whose characterization has been addressed in the previous sections, and of a strongly temperature and size dependent MNP property, the magnetic moment relaxation time τ, which also depends on MNP anisotropy, internal structure and hydrodynamic behavior. In this subsection SAR and related studies are reported. Measurements of the inversion field H_i versus maximum applied field H_{max} ($0 - 1.43 \ 10^6$ A/m) were performed at RT on selected samples, estimations of SAR were carried out using a two levels model for the MNP spin orientation state, and a comprehensive analysis of SAR experimental results is addressed.

Temperature T vs. time t curves were recorded for all samples for $H_0 \leq 57.7$ kA/m (see insets of figure 13a,b). Figure 13a shows the $\Delta T / \Delta t$ slope values of the linear initial region of the $T(t)$ curves recorded for the $D = 18$ nm, $x = 0.2$ (S2) sample while being irradiated with a 260 kHz RF field as a function of H_0^2. This initial linear response was observed for all samples indicating that during short periods of time ($t \leq 20$ s) our experimental device behaves almost adiabatically for ΔT of up to at least 20 K. The experimental SAR values were retrieved from the measured slopes using expression (Vergés *et al* 2008)

$$SAR = \frac{C}{\phi} \Delta T / \Delta t, \quad \phi = \frac{m_{MNP}}{m_{FF}}, \qquad (1)$$

where C is the FF specific heat and m_{FF}, m_{MNP}, are the masses of FF and MNP in the Dewar, respectively. A linear dependence on ferrofluid concentration $c = \phi \rho_{FF}$ (ρ_{FF} is the FF mass density) was observed for the range of studied FF concentrations $c \leq 12$ kg/m^3, as in the example

---

[5] For consistency with most reported data *SAR* values are given in W/g.

shown in figure 13b for $D = 16$ nm, $x = 0.1$ (S2). This result rules out effects of MNP interactions or aggregation on the measured SAR during RF irradiation. SAR vs H_0 behaviour was investigated in the range 18 kA/m $\leq H_0 \leq$ 57.7 kA/m and the quadratic H_0 dependence expected from the linear response theory (Rosensweig 2002)

$$SAR \approx \frac{\pi \mu_0^2 \rho M_s^2 V H_0^2 f}{3kT} \frac{\omega \tau}{1 + (\omega \tau)^2} \qquad (2)$$

was found to hold up to $H_0 \sim 41$ kA/m for all samples, as shown in figure 13a for $D = 18$ nm, $x = 0.2$ (S2). In eq. (2) ρ is the MNP density, V its volume, τ its magnetic moment relaxation time, and $\omega = 2\pi f$ is the field angular frequency. A tendency to saturation is observed for higher H_0 values. This effect originates from the saturation of the M vs H cycle area,

$$SAR = f\varepsilon_{cycle} = -f\mu_0 \oint_f MdH, \qquad (3)$$

where ε_{cycle} is the energy per mass unit dissipated in one cycle and $\oint_f$ indicates that the cycle is
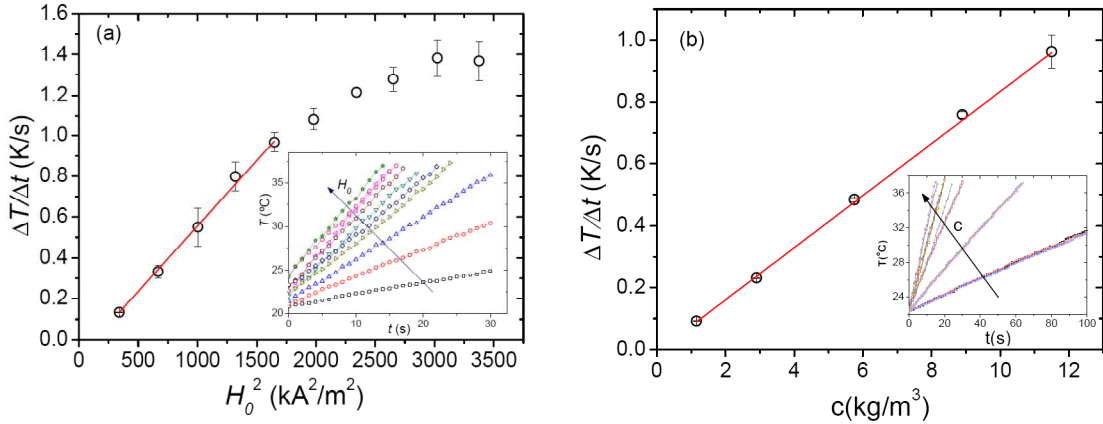

Figure 13.(a) Initial slopes $\Delta T/\Delta t$ for sample $D = 18$ nm, $x = 0.2$ (S2) as a function of H_0^2 showing a saturation effect for $H_0 > 41$ kA/m. (b) Dependence of the initial slope $\Delta T/\Delta t$ with FF concentration c for sample $D = 16$ nm, $x = 0.1$ (S2). Insets: initial linear region of $T(t)$ curves for field amplitudes 17 kA/m $\leq H_0$ ≤ 57.7 kA/m (a) and for concentrations 1 kg/m³ $\leq c \leq 12$ kg/m³.

performed at the RF frequency f.

Due to the lack of appropriate analytical expressions for evaluation of eq. (3) we have estimated SAR dependence on H_0 using a two energy levels model for the MNP magnetic moment orientation state (Carrey *et al* 2011). This estimation was performed for the $D = 18$ nm, $x = 0.2$ sample (S2). This model assumes uniaxial anisotropy and considers thermal activation transitions of the magnetic moment over the anisotropy energy barrier which separates opposite moment orientation states 1 and 2 (along the easy axis), disregarding moment oscillations around each of the

two energy minima. The assumption for Néel relaxation will be justified below, when we will conclude that this relaxation mechanism dominates for sizes $D \leq 18$ nm. When a field is applied parallel to the anisotropy axis the Zeeman and anisotropy interactions can be described as a function of the angle θ between the magnetic moment and the field as

$$E = KV \sin^2 \theta - \mu_0 V M_S H \cos \theta. \qquad (4)$$

For field values $|H| < H_K \approx 2K / \mu_0 M_S$ the energy barriers seen by moments oriented at angles $\theta = 0$ and $\theta = \pi$ have heights $E_{\pm} = KV(1 \pm h)^2$; where $h = H / H_K$. The frequency for the transition from level at $\theta = \pi$ to level at $\theta = 0$ is given by $v_1 = v_0 e^{-E_- / kT}$ and by $v_2 = v_0 e^{-E_+ / kT}$ for the opposite one. Calling P_1 to state 1 occupation probability, it follows the differential equation

$$\frac{dP_1}{dt} = v_1 - \frac{(v_1 + v_2)}{2} P_1. \qquad (5)$$

Taking into account that $d / dt = (d / dH)(dH / dt)$ and that $M = M_S(2P_1 - 1)$, eq. (5) becomes

$$\frac{dM}{dH} = \frac{2M_S \left\{ v_1 - \left(\frac{v_1 + v_2}{2} \right) \left(\frac{M}{M_S} + 1 \right) \right\}}{dH / dt}. \qquad (6)$$

Assuming for simplicity that the field is a triangular periodic function of time, dH / dt takes alternating constant values $\pm 4 f H_0$, and eq. (6) can be easily solved by numerical methods. From here, SAR can be evaluated using (3) for any frequency f and any field amplitude H_0. The assumption that the anisotropy axis be parallel to the applied field is a reasonable one if the relaxation mechanism is the Néel one and the frequency is not too high. Under these conditions energy minima are deeper for parallel orientation than for any other one and instantaneous energies are smaller, therefore leading to an effective orientation of the MNPs easy axes along the field. M vs H cycles, simulated for $f = 260$ kHz, $v_0 = 10^9 s^{-1}$, $K = 1.89 \ 10^4$ J/m^3, $V = 5.832 \ 10^{-24}$ m^3 (cubic MNP), $T = 310$ K and for increasing values of H_0 are shown in figure 14a, where a maximum inversion field $H_i^{RF} \approx 20.7 \ kA/m$ is observed. The dependence of SAR on field amplitude, calculated for the stated value of K as well as for $K = 2.47 \ 10^4$J/m^3, is presented in figures 14b and 14c, respectively. The fact that the experimental SAR values obtained for $H_0 = 41$ kA/m (see figure 17b) are at least six times smaller than those shown in figure 14 could be attributed, at least in principle, to the broad nanoparticle size distribution ($\sigma_D \sim 10$ nm, see below). On the other hand, a quasi linear dependence on H_0^2 is found for $H_0 < 25.1$ kA/m (figure 14b) and $H_0 < 39.8$ kA/m

(figure 14c), in agreement with the experimental results previously shown in figure 13a. The dependence on K of the field value at which the curve slope suddenly diminishes, reveals the influence of anisotropy on retarding SAR saturation effects.
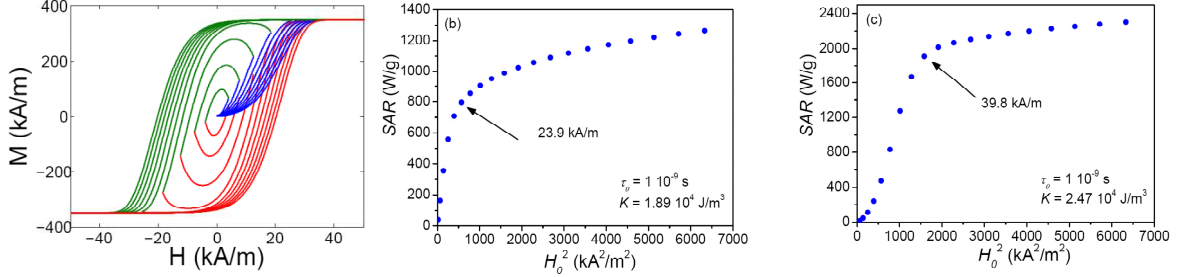

Figure 14. (a) M vs H loops calculated for the D = 18 nm, x = 0.2 sample (S2) as a function of field amplitude H_0 using the two levels approach for MNP moment Néel relaxation. (b),(c) SAR vs H_0^2 for two different values of anisotropy K.

The H_i^{RF} values obtained from the two levels model were in acceptable agreement with those estimated by frequency scaling H_i^{VSM} values measured with a VSM from minor M vs H cycles performed on the $D = 18$ nm, $x = 0.2$ sample (see figure 15). The scaling was performed assuming that the conditions under which $H_C(T) = H_C(0)\left\{1 - \sqrt{\alpha \ln(\tau_{obs}/\tau_0)}\right\}$ is valid (Cullity and Graham 2009) also apply for H_i,

$$H_i^{RF}(H_0) = \frac{1 - \sqrt{-\alpha \ln(f\tau_0)}}{1 - \sqrt{-\alpha \ln(f_{VSM}\tau_0)}} H_i^{VSM}(H_0), \qquad (7)$$

where $\tau_0 = \nu_0^{-1} = 10^{-9} s$, $\alpha = kT/KV$ and the "frequency" f_{VSM} was estimated from the VSM recording time τ_{VSM} as $f_{VSM} \approx \tau_{VSM}^{-1}$ ($\tau_{VSM} \sim 30$ s). The conversion factor from VSM to RF was ~ 13.4. We have found that H_i^{RF} values obtained with the two levels model are 61 % of those retrieved from H_i^{VSM} and eq. (7) as indicated in figure15.
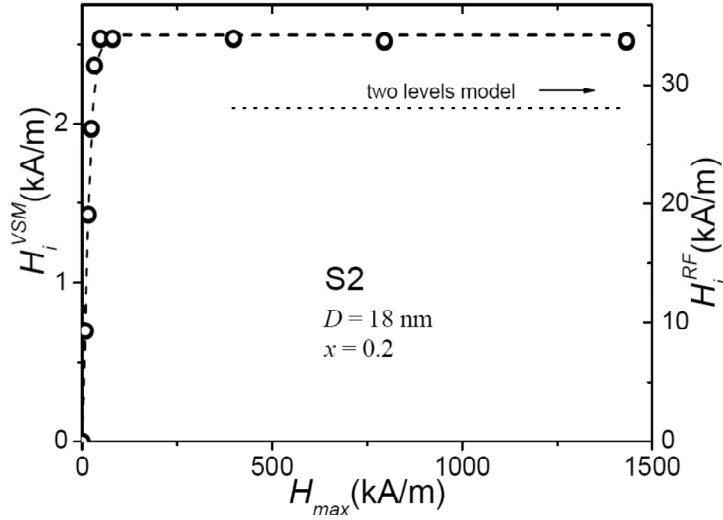
18

Figure 15. Inversion fields H_i^{VSM} retrieved from RT VSM minor loops recorded at $-H_{max} \leq H \leq H_{max}$ for the $D = 18$ nm, $x = 0.2$ sample (S2), and H_i^{RF} values calculated with eq. (7).The dashed line is a guide to the eye. The dotted line indicates the maximum H_i^{RF} value obtained with the two levels model.

SAR values obtained from FF of S1 MNPs in Chitosan suspension (viscosity $\eta \sim 6 \cdot 10^{-3}$ Pa s and specific heat $C \sim 4.2 \cdot 10^3$ J/kg K at RT), for different H_0 values between 18 kA/m and 57.7 kA/m, are shown in figure 16a as a function of x. In all cases the highest SAR occurs for $x = 0.0$, $D = 117$ nm, being 323 W/g the highest value for $H_0 = 41$ kA/m. The intrinsic loss power values $ILP = SAR /\left(H_0^2 f\right)$ are close to 0.5 nHm^2/kg, four to five times lower than recently reported results (Behdadfar et al 2012), probably due to the quite large size dispersion observed in our samples. Based on eq. (2), the behaviour is systematic and dominated by size through $V \approx D^3$ (see first factor of the expression) while the influence of τ cannot be appreciated. SAR values obtained from aqueous S2 FF, for $H_0 = 41$ kA/m, seem to present a more erratic behaviour with x (figure 16b), having a pronounced maximum value of 367 W/g at $x = 0.1$, $D = 16$ nm. In order to understand these results we come again to eq. (2), which shows that SAR is a function of several physical quantities from which the most inaccessible one is τ. This characteristics of τ arises from its dependence on τ_0 and K for Néel relaxation, or on the hydrodynamic volume V_h for Brown fluctuations $\left(\tau_B = 3\eta V_h / kT\right)$, since these magnitudes are difficult to determine precisely (τ_0, V_h), or have a strong dependency on the size of the nanoparticles (K). In order to gain more insight on

this we have normalized the whole set of SAR results (S1 and S2) by the factor $M_S^2 V H_0^2$ with the

aim of revealing the behaviour of $\dfrac{\omega\tau}{1+\left(\omega\tau\right)^2}$, which is essentially the frequency factor of the
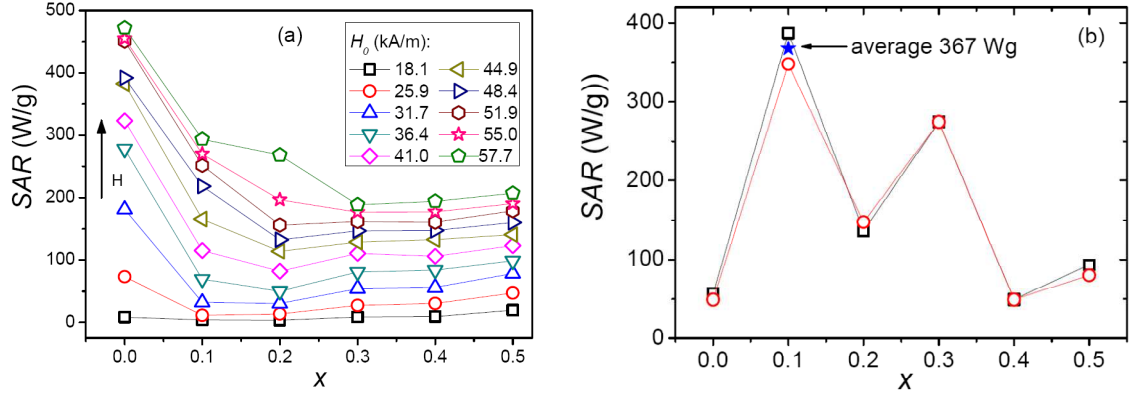

Figure 16. (a) SAR values as a function of x for set S1, for different field amplitudes H_0 indicated on the upper right. (b) Idem for set S2 obtained from SAR vs FF composition c (circles) and from SAR vs H_0 measurements (squares) and normalized for $H_0 = 41$ kA/m.

susceptibility dissipative component χ'. To this end the normalized data were forced to correspond

to a function with a maximum value of 0.5 in agreement with the frequency factor expression. The

result is presented in figure 17 as a function of MNP size and shows a consistent behaviour for the

whole set samples, S1 and S2. These data were analyzed assuming the possibility of both Néel and

Brown relaxation processes. For the first one values of $K = 1.89\ 10^4$ J/m^3 and $\tau_0 = 10^{-9}$ s were used,

and the existence of a dead magnetic layer of thickness t was considered, i.e., MNP size was set as

$D = D_C + 2t$, with $t \approx 2\,nm$. For the second relaxation mechanism, different values of η were
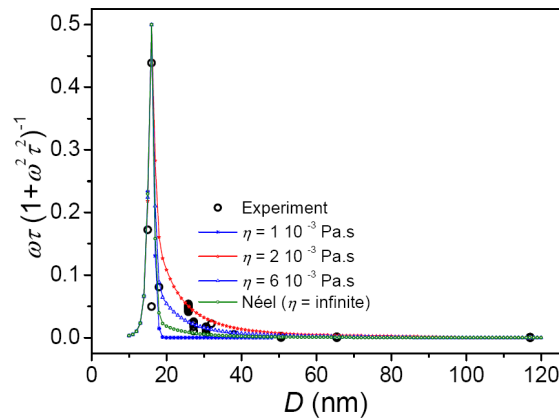

Figure 17. Dependence of the frequency factor of the dissipative susceptibility frequency factor $\omega\tau / 1+\left(\omega\tau\right)^2$ with MNP mean size for the whole set of samples S1 plus S2.

considered between $1\ 10^{-3}$ Pa s and $6\ 10^{-3}$ Pa s. The effective relaxation time was calculated with

$$\tau = \left(\frac{1}{\tau_N} + \frac{1}{\tau_B} \right)^{-1}$$ were indexes N and B stand for Néel and Brown processes, respectively. A

reasonable agreement was found between the experimental data and the simulations represented in figure 17 by full lines. The best description was achieved for an intermediate value of $\eta \sim 2\ 10^{-3}$ Pa s. This is an acceptable value bearing in mind that most of the results come from Chitosan suspended FF (S1). Chitosan solution has a viscosity of $6\ 10^{-3}$ Pa s at 293 K, but it is well known that liquids viscosity drops rapidly with temperature, thus making this result plausible. Most S2 samples, suspended in water, have sizes below the one from where the Brown mechanism dominates (~ 18 nm, figure 18) and therefore do not influence so much the overall behaviour of the normalized SAR values in the Brown relaxation region.

The RT relaxation time τ dependence on particle size D was calculated with the stated values of τ_0, K and t, for the two extreme η values: $1\ 10^{-3}$ Pa s and $6\ 10^{-3}$ Pa s (see figure 18). It can be seen that 13 nm – 14 nm MNP have relaxation times (Néel process) of the order of the Mössbauer observation time window, in agreement with what was inferred on the basis of the fast relaxing contribution spectral areas.
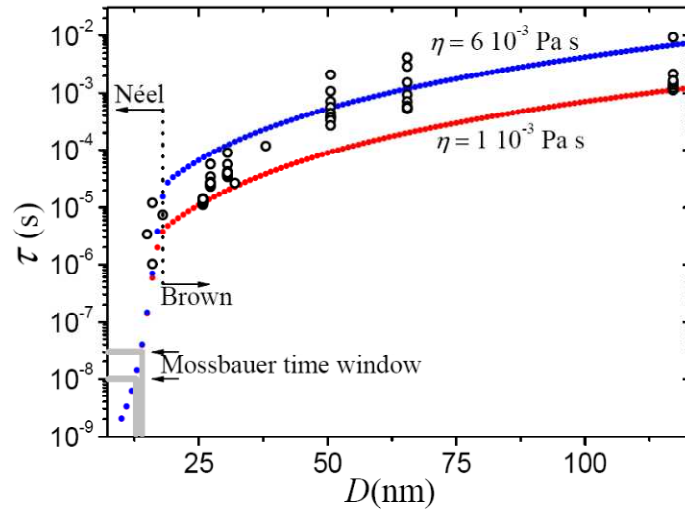

Figure 18. Open large dots: experimental relaxation times obtained from $\omega\tau / 1 + (\omega\tau)^2$ (figure 17). Filled small dots: values calculated by considering the possibility of both Néel and Brown relaxation mechanisms, for two different viscosity values.

Experimental relaxation times retrieved by solving $\omega\tau \left(1 + (\omega\tau)^2 \right)^{-1}$ (figure 17) for τ, are in good agreement with the assumed model and are shown as open circles in figure 18. Figure 19 shows the

subset of experimental values retrieved using $H_0 = 41$ kA/m plotted in a log-log scale. The straight line fitted to this data subset has a slope of -3.2 ± 0.3, which reflects the dominance of the Brown relaxation process for $D \geq 18$ nm $\left(\log \tau_B \propto 3D\right)$.
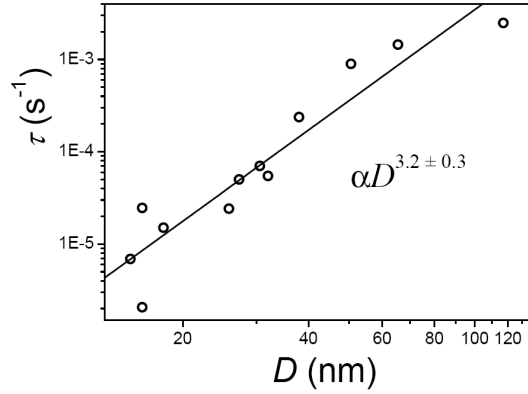

Figure 19. Log-log view of the subset of experimental relaxation times obtained using $H_0 = 41$ kA/m. The full line is the result of a linear fit of the data and has a slope of 3.2 ±0.3 revealing that NP moment relax by the Brown mechanism for $D \geq 18$ nm.

4. Summary and conclusions

A detailed study of $Zn_xFe_{3-x}O_4$ ($0.0 \leq x \leq 0.5$) cubic like MNPs obtained by chemical coprecipitation, as well as on their water and Chitosan based ferrofluids, was conducted. By modifying synthesis conditions and Zn concentration the mean size D of MNPs could be varied between 15 nm and 117 nm.

Mössbauer effect spectroscopy, XAS and dc magnetization results indicate that Zn^{2+} ions enter selectively at the spinel A sites.

For $D \leq 32$ nm important magnetic relaxation effects were observed by Mössbauer effect at room temperature. Two relaxing contributions were needed for spectral analysis. One of them (fast relaxing component) corresponded to probes experiencing relaxation times $\tau < \tau_L$, i.e. located in MNPs with individual sizes smaller than the RT Mössbauer blocking size $D_B \sim 13\text{-}15$ nm, which experience a null effective B_{hf}. The other one (slow relaxing component) corresponded to probes experiencing relaxation times of the order of τ_L, located in MNPs of the order of 15 nm. The pattern associated to this component reveals that the involved Fe probes experience a non zero B_{hf}, and that they are located exclusively at B sites. The B_{hf}^B at non relaxing ^{57}Fe probes located at B sites experiences a strong diminution and becomes increasingly distributed as Zn^{2+} is gradually

incorporated, selectively and randomly at *A* sites, due to the multiplicity of different metal neighbour configurations created around the ^{57}Fe probes. On the other hand B_{hf}^{A} experiences only minor changes while its associated spectral area decreases steadily as Fe is replaced by Zn at the *A*-sites.

Magnetization was observed to increase with Zn concentration for $x \leq 0.1$ - 0.3 independently of the size range, however the relative enhancement was significantly larger in the case of the MNP S2 batch where average sizes were smaller ($D \leq 38$ nm). Saturation magnetization increase was interpreted in terms of deactivation of Fe^{3+} moment cancellation at neighbouring *A* and *B* sites, due to Zn^{2+} incorporation at *A* sites and local switching off of *A-B* superexchange. This mechanism produces a net moment of 10 μ_B at the unit formula where Zn^{2+} has been incorporated, instead of the 4 μ_B observed in pure magnetite. On the other hand, magnetization deterioration for *x* > 0.3 also obeys to the weakening of the *A* – *B* superexchange interaction and the consequent takeover of the *B* – *B* one when Zn^{2+} *A* site occupation is high , thus leading to null atomic moment at the unit formula where Zn^{2+} is located.

SAR was measured in water and Chitosan based ferrofluids using a 260 kHz RF field. Experimental results could be interpreted within the frame of the linear response theory for field amplitudes $H_0 \leq 41$ kA/m. Results obtained at a constant $H_0 = 41$ kA/m depended both on *x* and *D*, displaying a maximum value of 367 Watts per gram of MNPs for $D = 16$ nm and $x = 0.1$. A departure towards a saturation regime was observed for higher fields. This saturation effect was understood using a two levels approximation for the Néel magnetic moment relaxation which was solved numerically. In addition, this model revealed that increasing MNP effective anisotropy would improve magnetic hyperthermia performance at higher fields by shifting upwards the H_0 limit up to which the quasilinear SAR vs H_0^2 dependence holds. The frequency factor of the susceptibility dissipative component was retrieved by normalizing SAR by its expected volume, field amplitude and saturation magnetization dependences. This quantity, $SAR/M_S^2 V H_0^2$, presented a sharp maximum at $D \sim 16$ nm, which corresponds to the resonant Zn-doped magnetite MNP size for the working frequency of $2.6 \ 10^5$Hz. Normalized SAR was converted into the frequency factor $\omega\tau\left(1+(\omega\tau)^2\right)^{-1}$ by further normalization, from where experimental values of the relaxation time were obtained. These experimental τ values compare satisfactorily with those calculated for Néel and Brown moment reorientation mechanisms. The analysis is consistent with the existence of a crossover from Néel to Brown mechanisms at $D \sim 18$ nm.

The present study indicates that in cubic-like Zn-doped magnetite MNPs at RT and at $f = 2.6 \; 10^5$ Hz, the MNP size for maximum $\omega\tau\left(1+\left(\omega\tau\right)^2\right)^{-1}$ is $D \sim 16$ nm. However, the best SAR values of the whole set of samples corresponded, in order of performance, to mean sizes of 18 nm ($x = 0.1$, S2), 117 nm ($x = 0.0$, S1) and 32 nm ($x = 0.3$ S2). This departure from the size corresponding to maximum $\omega\tau\left(1+\left(\omega\tau\right)^2\right)^{-1}$ is due to the influence of saturation magnetization and MNP volume on SAR, through the $M_S^2 V$ factor in eq. (2). In the case of the present work, volume through its D^3 dependence becomes an important factor due to the wide range of NP mean size values. However, the increase in D^3, for instance of almost 400 times from 16 nm to 117 nm samples, is approximately compensated by the dramatic decrease of the frequency factor $\omega\tau\left(1+\left(\omega\tau\right)^2\right)^{-1}$. To get advantage of this D^3 factor, frequency should be shifted to a lower value, i.e. the one which makes 117 nm the resonant size. But this would bring about a drawback, since the first factor of SAR in eq. (2) depends linearly on frequency. Therefore high enough frequencies in the range of 10^5 to 10^6 Hz have to be used in order to attain efficient SAR performance. This scenario leads us to the conclusion that in order to improve the SAR performance of magnetite based materials, and approach or surpass the 1 kW/g goal, it is necessary to enhance M_S while making D of the order of the resonant size corresponding to the working frequency.

Acknowledgements

References

Behdadfar B, Kermanpur A, Sadeghi-Aliabadi H, Morales M P, and Mozaffari M 2012, Journal of Magnetism and Magnetic Materials 324, 2211–2217.

Brezovich I A in Biologcal, Physical and Clinical Aspects of Hyperthermia, ed. by B.R. Paliwal, F.W. Hetzel and M.W. Dewhirst, Medical Physics Monograph No. 16, 1987, 82 – 110.

Carrey J, Mehdaoui B, and Respaud M 2011, Journal of Applied Physics 109, 083921.

Cullity B D and Graham C D 2009, *Introduction to Magnetic Materials*, Wiley, p. 388.

Fiorani D, Testa A M, Lucari F, D'Orazio F and Romero H 2002, Physica B, 320, 122–126.

Fortin J-P, Gazeau F and Wilhelm C 2008, Eur Biophys J, 37:223–228.

Gneveckow U, Jordan A, Scholzc R, Brüß V, Waldöfner N, Rickef J, Feussner A, Hildebrandt B, Rau B, and Wust P 2004, Medical Physics, Vol. 31, No. 6, 1444-1451.

Häfeli U O, Aue J, Damani J 2007, The biocompatibility and toxicity of magnetic particles in *Laboratory Techniques in Biochemistry and Molecular Biology*, *32*, *Pages 163-223*

Hergt R, Hiergeist R, Zeisberger M, Schüler D, Heyen U, Hilger I, Kaiser W A 2005, Journal of Magnetism and Magnetic Materials 293, 80–86.

Hergt R, Dutz S, Müller R and Zeisberger M 2006, J. Phys.: Condens. Matter 18, S2919–S2934.

Kaiser R and Miskolczy G 1970, Journal of Applied Physics, 41, 1064-1072.

Kim D K, Zhang Y, Voit W, Rao K V and Muhammed M 2001, Journal of Magnetism and Magnetic Materials 225, 30-36.

Knobel M, Nunes W C, Socolovsky L M, De Biasi E, Vargas J M, and Denardin J C 2008, Journal of Nanoscience and Nanotechnology, Vol.8, 2836–2857.

Lutterotti L 2010, Nuclear Inst. and Methods in Physics Research, B, 268, 334-340.

Maier-Hauff K, Ulrich F, Nestler D, Niehoff H, Wust P, Thiesen B, Orawa H, Budach V, Jordan A 2011, J Neurooncol, 103, 317–324

Nakashima S, Fujita K, Tanaka K, Hirao K, Yamamoto T, Tanaka I 2007, Phys. Rev. B 75, 174443.

Overggard J. 1989, Int J Radiation Oncology Biol Phys; 16:535-549

Pankhurst Q A, Thanh N K T, Jones S K and Dobson J 2009. "Progress in applications of magnetic nanoparticles in biomedicine" J. Phys. D: Appl. Phys. 42, 224001 (15pp).

Ravel B and Newville M 2005, J. Synchrotron Rad., 12:4, 537-541.

Rosensweig R E 2002, Journal of Magnetism and Magnetic Materials 252, 370–374.

Sorensen C M 2001, in Nanoscale Materials in Chemistry, edited by K. J. Klabunde Wiley, New York, p. 169.

Stewart S J, Figueroa S J A, Ramallo López J M, Marchetti S G, Bengoa J F, Prado R J, Requejo F G 2007, Phys. Rev. B 75, 073408-073411

Tasaki J and Izushi T 1977, Journal de Physique Colloque C1, supplment au no 4, Tome 38, page C1-175.

Vandenberghe R E and de Grave E 1989, *Mössbauer Effect Studies of Oxidic Spinels*, in *Mössbauer Spectroscopy Applied to Inorganic Chemistry*, edited by G. J. Long and F. Grandjean sPlenum, New York , Vol. 3, pp. 59–182.

Vandenberghe R E, Barrero C A, Da Costa G M, Van San E, De Grave E 2000, Hyperfine Interactions, 126, 247-259.

Vergés M A, Costo R, Roca A G, Marco J F, Goya G F 2008, Journal of Physics D: Applied Physics 41, 134003.

Wen M, Li Q, and Li Y 2006, J. Electron Spectroscopy and Related Phenomena 153, 65-70.

Supplementary Data

EXAFS results

Room temperature near-edge x-ray absorption fine structure (XANES) and extended x-ray absorption fine structure (EXAFS) spectra of the Fe K-edge (7112 eV) and Zn K-edge (9659 eV) were recorded in transmission mode using a Si (111) monochromator at the XAS beamlines of the LNLS (Laboratorio Nacional de Luz Sincrotron) in Campinas, Brazil. The spectra analysis was performed by pre-edge background subtraction followed by a normalization procedure considering the EXAFS region. The fine structure oscillations $\chi(k)$ of each spectrum in the extended region were isolated using the ATHENA program (Ravel and Newville 2005) and Fourier transformed over a specific k range (2 to 10 Å^{-1}).

The following figures shows the Fourier transform (FT) of $k^2\chi(k)$ EXAFS at Zn and Fe K-edges without phase correction. The fit results are summarized in Table 1.
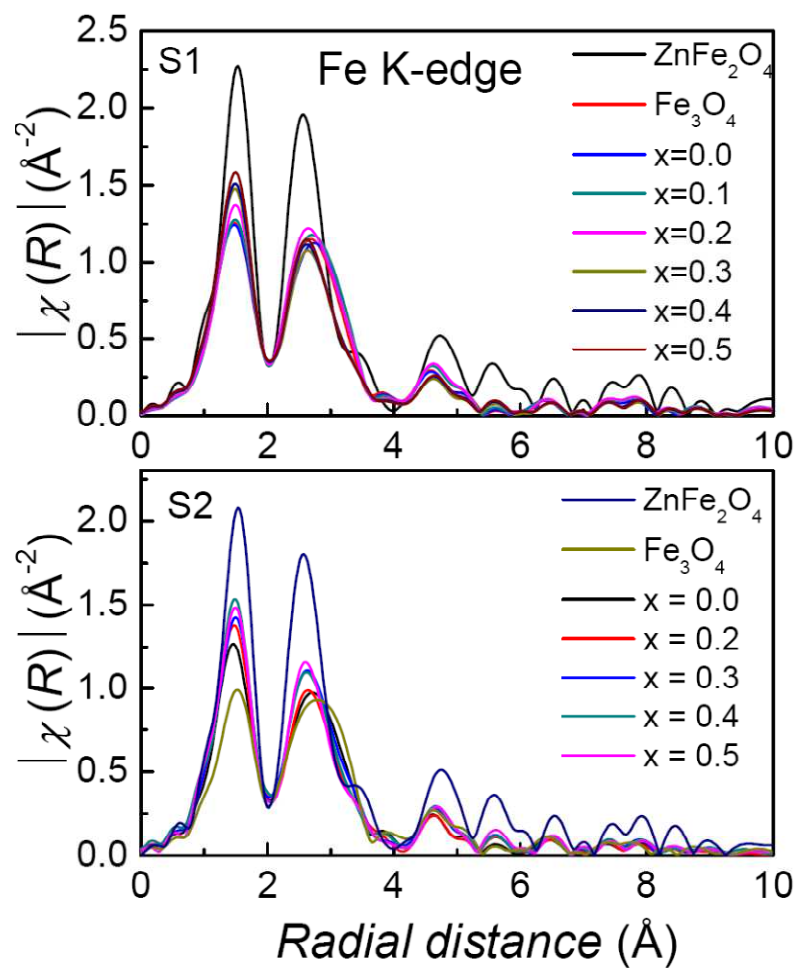
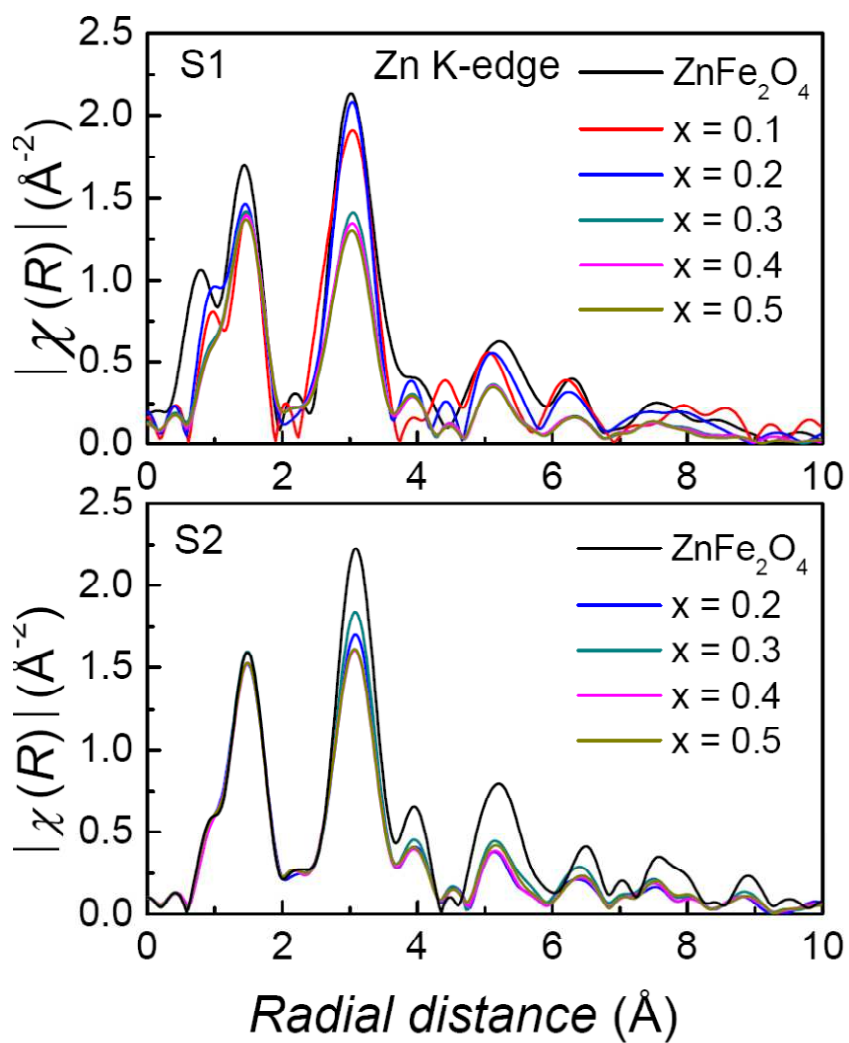*Figure 1. Fourier transforms of EXAFS data at Fe K-edge for S1 and S2 series.*

Figure 2. Fourier transforms of EXAFS data at Zn K-edge for S1 and S2 series.

Table 1. EXAFS Fe and Zn K-edges fitted parameters assuming a first coordination shell of oxigens. N is the coordination number, R the distance from central atom and σ^2 the Debye-Waller factor.

Serie	Edge	Sample	N	R (Å)	σ^2 (Å^2) x 10^{-3}
		Fe_3O_4	5.4(2)	1.985(7)	12
		$ZnFe_2O_4$	6.0	2.004(2)	4
		x=0.0	5.5(2)	1.987(8)	12
		x=0.1	5.5(2)	1.996(7)	12
	K-Fe	x=0.2	5.5(2)	1.996(5)	11
		x=0.3	5.5(1)	1.980(3)	10
S1		x=0.4	5.6(1)	1.984(3)	9
		x=0.5	5.7(1)	1.985(3)	9
		$ZnFe_2O_4$	3.8(1)	1.96(1)	2
		x=0.1	3.4(5)	1.94(2)	5
	K-Zn	x=0.2	4.0(3)	1.96(1)	6
		x=0.3	3.9(2)	1.966(7)	6
		x=0.4	3.8(2)	1.971(7)	5
		x=0.5	3.9(2)	1.971(7)	6
		x=0.0	5.6(2)	1.969(8)	12
		x=0.2	5.8(1)	1.973(4)	11
	K-Fe	x=0.3	5.7(1)	1.986(2)	10
		x=0.4	5.8(2)	1.979(6)	10
S2		x=0.5	5.4(1)	1.981(2)	8
		x=0.0	3.8(2)	1.969(7)	4
		x=0.2	4.1(2)	1.970(9)	5
	K-Zn	x=0.3	3.8(2)	1.966(7)	4
		x=0.4	3.9(2)	1.971(7)	5
		x=0.5	3.8(2)	1.975(7)	5

References

Ravel B. and Newville M. 2005, J. Synchrotron Rad. 12, 537.